

Appendix: The Science Case and Instrumentation for Extra Large Telescopes

E. Barton Gillespie (NRC/HIA), R. Carlberg (Toronto), T. Davidge (NRC/HIA), JJ Kavelaars (McMaster), D. Crabtree (NRC/HIA), M. Hudson (Waterloo), J. B. Oke (NRC/HIA), C. L. Morbey (NRC/HIA), R. G. Abraham (Toronto), L. Jolissaint (NRC/HIA), J.-P. Veran (NRC/HIA), J. P. Fulbright (NRC/HIA), P. B. Stetson (NRC/HIA), D. Bohlender (NRC/HIA)

ABSTRACT

In this appendix, we describe the detailed simulations and sensitivity estimates used to define the scientific goals of an extra large optical telescope.

Contents

1	Introduction	2
2	Planet Detection	3
3	Imaging Resolved Stellar Populations	5
3.1	Stars in Nearby Galaxies	5
3.1.1	Why study resolved stars in nearby galaxies?	5
3.1.2	Probes of Stellar Content	5
3.1.3	RR Lyrae Stars	6
3.2	White Dwarf stars in the Milky Way Galaxy	6
4	The Morphologies of Distant Galaxies	8
5	The Formation of Galaxies and Large-scale Structure at $z \sim 3$	8
5.1	Motivation	8
5.2	Goals	11
5.3	Survey Parameters	11
6	The Evolution of Galaxies	11
6.1	Chemical Evolution of Galaxies	13

6.2	Internal Kinematics at Intermediate Redshift	13
6.3	Very Distant and Young Objects: “Lyman Break” Galaxies and Beyond	17
6.4	The First Star Formation in the Universe	17
7	High-resolution Stellar Spectroscopy	17
8	Performance Calculations	20
8.1	Formulas for Signal-to-Noise Calculations	20
8.1.1	Imaging	22
8.1.2	One-Dimensional Spectroscopy	22
8.1.3	Two-Dimensional Spectroscopy	23
8.2	Sensitivity of a Broad-band Imager to Point Sources	23
8.3	Sensitivity of a Natural Seeing Multi-object Spectrograph	26
8.4	Sensitivity of a Natural Seeing High-resolution Spectrograph	26
8.5	Sensitivity of an Integral Field Unit Spectrograph with Adaptive Optics	26
9	Instrumentation: A Low-Resolution Multi-Slit Spectrograph for 20-30 Meter Telescopes	26
9.1	Design Approach	31
9.2	Straight-Through Spectrograph design	31
9.3	The Array of Cells	31
9.4	Slitmasks	34
9.5	Performance Expected	34
9.6	Flexibility	35
9.7	Weight and Cost for the 20-Meter Telescope Spectrograph	35

1. Introduction

In this early phase of design and planning for the next generation of extra large telescopes (XLTs), characterization of the the desired science performance and instrument complement are crucial for designing the goals and scope of the proposed projects. This task is a difficult one: history

shows that preliminary studies fail to identify all of science, or even the most important science, that a telescope will ultimately produce. However, there are still compelling reasons to pursue studies of the scientific capabilities of an XLT. Target science goals are absolutely necessary in order to form a basis for engineering decisions about the telescope and instruments. This science/engineering interchange will assure that the telescope is able to perform when it is finished.

This document presents an outline of the existing Canadian effort to explore the science cases and possible instrumentation for XLTs. The main focus is to differentiate the scientific capabilities of 20 and 30-meter telescopes and to explore the needed image quality and field of view. Secs. 2 – 7 discuss planet detection, imaging of resolved stellar populations, distant galaxy morphology, large redshift surveys, studies of the internal dynamics and chemistry of individual galaxies, and high-resolution stellar spectroscopy. In Sec. 8, we describe the detailed sensitivity calculations used throughout. Sec. 9 contains a design of a wide-field multi-object spectrograph.

2. Planet Detection

The discovery of a life-supporting planet orbiting a remote star is very likely to be counted among the great discoveries of the 21st century. Detection and investigation of extra-solar planetary systems has long been beyond the realm of the technically possible. Pioneering efforts by Canadian astronomers led to the development of instrumentation methods that have proven crucial to the current detections of giant planets orbiting our stellar neighbours. Ongoing efforts within Canada and abroad are ushering in the era of extra-solar planetary science.

We, as a society, have the technical ability to construct a telescope/detection system that will permit the observation and study of extra-solar planets. New, specialized coronagraphic detectors are being developed for the existing suite of 8-meter telescopes. However, these new precision-machined optical devices will not allow the observation of Earth sized bodies near their bright stellar companions.

Detection, by reflected light, of Extra-Solar Planets (ESPs) is not an extension of what is already doable using 8-meter telescopes. Three technical challenges must be met to allow the detection of ESPs.

1. Resolution: ESP targets of interest are between 3 and 10 pc away. For a star/planet separation of 1AU (to allow the investigation of the currently known suite of ESPs) requires resolutions better than $0.3''$. Of the approximately 60 known ESPs only 10 are separated from their parent stars by more than $0.1''$ and NONE are separated by more than $1''$.
2. Dynamic Range: Jupiter is 25 magnitudes fainter than the SUN. Thus, we must be able to observe a 0th magnitude star with a 25th magnitude companion. Differential coronagraphs being built for the 8-meter telescopes (like GEMINI) will allow differential fluxes of approximately 17 magnitudes. Although impressive, there are no known targets with separations

large enough for this instrument.

3. Flux limit. Objects at large separation from their parent stars (which would make excellent targets for the 8-meters) are, unfortunately, very faint. The star Epsilon Eridani is thought to have Neptune sized companion orbiting with a semi-major axis of 40 AU. Thus the angular separation and differential flux are not problematic. However, this planet, which is 40 AU from its parent star, has an expected luminosity of $H=30$, clearly well beyond the reach of the 8 meters.

From a planet-detection viewpoint, a large telescope will have two goals. First, we must provide a facility that will allow the precise modeling and monitoring of the menagerie of known extra-solar giant planets. Already, the detection and tracking of these systems has changed the perceptions of our own solar-systems formation and evolution. However, without the ability to investigate the atmospheric and chemical properties of these extra-solar systems, we will be left guessing about the ways in which planets form and evolve.

Our solar system provides a single example of a planetary system, wholly insufficient for properly understanding the formation of planetary systems. The second challenge is the direct, unresolved detection of Earth like planets orbiting other stars. Here too, we will turn to precise spectroscopic study to allow the determination of the physical properties of these yet-to-be-discovered planetary systems. These goals require a high resolution coronagraphic capability combined with high resolution/high signal-to-noise spectroscopy.

The daunting challenge of planet detection is the large differential in flux between the star and its planetary companion. The integrated H-band luminosity of Jupiter is 20 magnitudes lower than that of the Sun. To overcome this large differential requires a coronagraphic imager that can remove both the stellar PSF and the speckle pattern. Designs for coronagraphs are now being implemented for 8-meter class telescopes. However, the latest developments in coronagraphs on 8-meter class telescopes can only detect objects exterior to a few arc seconds from the planet. There are NO currently known extra-solar planets more distant than $1.1''$ from their parent star. However, these new high precision coronagraphs mounted on a 20-meter facility should be able to detect faint companions within $1''$.

The current bias towards massive, close-in planets is the result of the Doppler detection method. Direct imaging of a stellar system via a 20-meter telescope will allow detection of faint companions which are distant from the central stars, allowing the study of planetary systems that have been discovered by Doppler surveys. However, the more distant these planets are from their stellar parents, the dimmer they appear. A Neptune sized planet is suspected to be orbiting 40 AU from Epsilon Eridani (3.3 pc distant from the Sun). This planet could be easily resolved from its stellar host. However, the reflected flux from the planet is $m_H = 28.5$ magnitudes, far beyond the reach of the 8-meters. However, a 20 to 30 meter telescope equipped with a high precision coronagraph will allow the study of planets like the one suspected to be orbiting Epsilon Eridani.

3. Imaging Resolved Stellar Populations

3.1. Stars in Nearby Galaxies

3.1.1. *Why study resolved stars in nearby galaxies?*

One of the main goals of astronomy is to develop an understanding of galaxy evolution. Ideally, one would like to derive the star formation rate as a function of time for galaxies spanning a range of morphological types, and the most straight-forward way to do this is to study galaxies over a range of redshifts. However, there are difficulties studying the stellar contents of both distant and nearby galaxies. Distant galaxies are faint and not well resolved, so that one must rely on integrated properties, such as broad-band colours, to probe stellar content. A further complication is that at large redshifts the portion of the spectrum observed at visible wavelengths samples light from the rest frame ultraviolet, so that information is only obtained about the most recent episodes of star formation.

Nearby systems can be resolved into individual stars, so that stellar content can be probed in a direct manner; this is especially important for lifting the age-metallicity degeneracy that plagues integrated light studies. Sub-structures within a galaxy can also be probed, so that a picture of the relative histories of various components, such as the bulge, disk, and halo, can be established. Moreover, many resolved bright stars are standard candles, and hence can be used to measure distances. Nevertheless, nearby galaxies do not provide a panacea for galaxy evolution as these objects are observed well after they formed, and the location of stars at the current epoch may have been affected by dynamical processes, such as merging. Evolutionary processes may also alter the observed properties of individual stars; for example, mixing or dredge up can cause the surface chemical composition to be altered from the original values. Finally, we have an incomplete understanding of stellar evolution, with the uncertainties becoming greater towards more evolved states. As a result there is still not a reliable theoretical calibration relating observational properties (brightness, colour, line strengths) to astrophysically interesting quantities such as age and chemical content. Clearly, these uncertainties also affect our ability to model the integrated properties of distant systems.

3.1.2. *Probes of Stellar Content*

The basic properties of stars that can be used to probe stellar content in nearby galaxies are shown in Table 1. The second column indicates if the star is appropriate for investigating young (Y), intermediate-age (I), or old (O) populations. The brightnesses listed in the fourth and fifth column are typical values. The entries in the sixth column show the number of objects of this type that would be expected in a population with $M_V = -10$. Given that one of the main motivations for compiling the data in this table was to summarize parameters useful for constructing realistic models of galaxies, the number densities were estimated from observations of real composite systems

whenever possible. The entries for Cepheids and red and blue supergiants are taken from the LMC, and hence are representative of what would be seen in a dwarf Irregular galaxy. The AGB-tip and RGB-tip entries are based on the densities of objects seen in M32, and hence are applicable to spheroidal systems. The remaining stars are much fainter, and so the number entries for these objects have been based on observations of globular clusters.

Fig. 1 shows simulated images of the stellar populations of M31, Virgo, and Coma galaxies. The M31 and Virgo simulations are for a 3 hour total integration time, while the Coma cluster simulation is for a 3 night integration time. The simulations assume a 20-meter aperture and an AO-corrected PSF with a Strehl of 0.3. The M31 simulation includes stars on the AGB, RGB, HB, and SGB; the AGB and RGB stars are distributed along these sequences assuming a luminosity function power-law exponent of 0.3. The Virgo cluster simulations include the AGB, RGB, and HB components, while the Coma simulation includes only the AGB and RGB; as with M31, the AGB and RGB stars are distributed in brightness with a power-law luminosity function. The brightest stars in each simulation are objects evolving near the AGB-tip, which have $M_K = -9$. These simulations indicate that stars as faint as the SGB can be resolved with a 20 meter telescope well inside the bulge of M31, while stars on the upper RGB can easily be resolved in Virgo. Finally, with long (i.e. multi-night) integrations it will be possible to resolve the brightest stars in Coma cluster galaxies. Hence, a large volume of the Local universe can be resolved into stars with a 20 meter telescope equipped with an AO system.

3.1.3. *RR Lyrae Stars*

Only very old, metal-poor stellar populations can produce the distinctive variable stars of the RR Lyrae type. These stars typically have periods of one-quarter to three-quarters of a day, and can have amplitudes in excess of one magnitude. Therefore they are easily recognizable tracers of the first generation of star formation in nearby galaxies. Furthermore, since it is possible to define the absolute magnitudes of RR Lyraes found in the Solar Neighborhood, in Galactic globular clusters, and in the Magellanic Clouds, these stars can provide a Population II distance ladder to nearby galaxies that is independent of Population I distance indicators, such as Cepheid variable stars. RR Lyrae stars are comparatively hot, and their light variation is most pronounced at shorter wavelengths, so they are far more profitably studied at optical wavelengths rather than in the infrared. A well equipped Large Optical Telescope would be able to discover and measure RR Lyrae variables in galactic haloes out to distances of order 10 Mpc.

3.2. **White Dwarf stars in the Milky Way Galaxy**

Stars of order one Solar mass end their lives as white dwarfs. Recent sophisticated models of white dwarfs have led to the prediction that in dense, hydrogen-rich white dwarf atmospheres,

Table 1.

Object	Age	Standard Candle?	M_V	M_K	Number	Comments
Blue Supergiant	Y	Yes	-7 ^a	-6	0.01 ^a	
Red Supergiant	Y	Yes	-9.5 ^a	-9 to -12	0.02 ^a	
Cepheid	Y	Yes	-1 to -7	-2.5 to -9	1.0 ^b	Primary diagnostic for distance.
AGB-tip	I, O	Yes	0 to -2	-6 to -9	4.0 ^c	
RGB-tip	I, O	Yes	0 to -3	-6 to -7	100 ^c	
HB	O	Yes	1	1 to -1.5	4000 ^d	
Sub-giant branch	O	No	2 to 4	0 to 2	10000 ^e	
Main sequence turn-off	Y, I, O	No	5 (old population)	3 (old population)	100000 ^f	Primary diagnostic for age.

^aBased on the top mag of each phase in Figure 3 of Humphreys & McElroy (1984, ApJ, 284, 565)

^bAlcock et al. 1999, AJ, 117, 920

^cFrom M32 outer field of Davidge (2000, PASP, 112, 1177), for top 1 mag in K for each sequence, assuming that 25% of stars in the top mag of the RGB are on the AGB

^dComputed assuming $dN/d\text{Log}K = 0.3$ (Davidge 2001, AJ, in press) and $R = 1.4$ (Buzzoni et al. 1983, A&A, 128, 94)

^eFrom Davidge & Courteau (1999, AJ, 117, 1297) LF of M92, where number of SGB stars is roughly 2.5 times that in the bottom 0.5 mag bin of the RGB

^ffrom K LF of M4 (Davidge & Simons 1994, ApJ, 423, 640)

molecular hydrogen should form. This molecular hydrogen will be quite opaque in the red and infrared portions of the spectrum, which will squeeze the white dwarfs’ radiative cooling into the visible and blue wavelengths. As a result, white dwarfs older than about 9 or 10 Gyr will become progressively bluer as they age, and they will maintain a nearly constant absolute visual magnitude of order 17.5 until ages of 15 Gyr or more. This means that hydrogen-rich white dwarfs belonging to the nearest dozen or so Galactic globular clusters — the oldest recognizable stellar systems — will be virtually undetectable in the red and infrared, but they should be accessible to an Extra Large Telescope. They will yield a new and robust determination of the absolute age of the Milky Way Galaxy, the extent of its formation phase, and the relative timing of the first metal-poor and metal-enhanced populations.

4. The Morphologies of Distant Galaxies

Galaxy morphologies, as measured in optical and near-infrared images, hold important clues to the structure, composition, and evolution of galaxies outside the Milky Way. *Direct* measure galaxy evolution as a function of redshift requires the detection and characterization of faint features.

Extra large optical telescopes promise to improve our view of the early Universe with both greater collecting area and superior image quality. Fig. 3 shows the vast improvement in images of distant galaxies possible with a large optical telescope. The figures show simulations of distant interacting galaxies as they participate in a close pass and finally merge. The tidal tails in the middle panel are barely visible through 4-meter class telescopes like CFHT, even with very long exposures. In contrast, the 20-meter XLT optical telescope shows the tails quite clearly, along with the “globular clusters” (unresolved dots) present in the simulation. Tidal tails are important indicators of galaxy interaction, and can be used to constrain the mass distributions of dark matter halos in interacting galaxies directly (as in Dubinski, Mihos, & Hernquist 1999, ApJ, 526, 607). Photometry of globular clusters can provide, among other constraints, important fossil information about the merging history of massive galaxies.

5. The Formation of Galaxies and Large-scale Structure at $z \sim 3$

5.1. Motivation

Current results indicate that most of the star formation in the Universe occurs between redshifts 1 and 3. Steidel and collaborators have successfully identified $\sim 10^3$ luminous star-forming ($4\text{--}20 M_{\odot}/\text{year}$) galaxies at $z \sim 3$. These galaxies are highly clustered, with biasing factors estimated in the range 2 – 4. The comoving volume density of these Lyman-break galaxies is low, somewhat less than present-day L_{\star} galaxies. Furthermore, the Steidel sample sees only the brightest 20% of the star formation. The spectral resolution is low, approximately 10-12 Å or 3 Å in the rest frame,

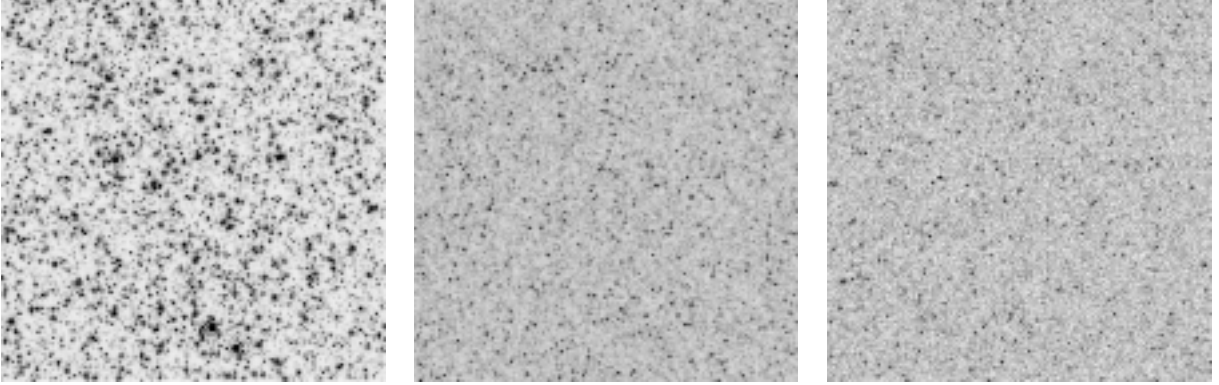


Fig. 1.— Synthetic K' images generated using the IRAF artdata routine and the information shown in Table 1. The images are for a field in the bulge of M31 with a surface brightness in V of 17.9 (left), a field in a Virgo elliptical with $\mu_V = 19.5$ (middle), and a Coma cluster elliptical with $\mu_V = 23.5$ mag. per square arcsec (right). See the text for a description of the simulations.

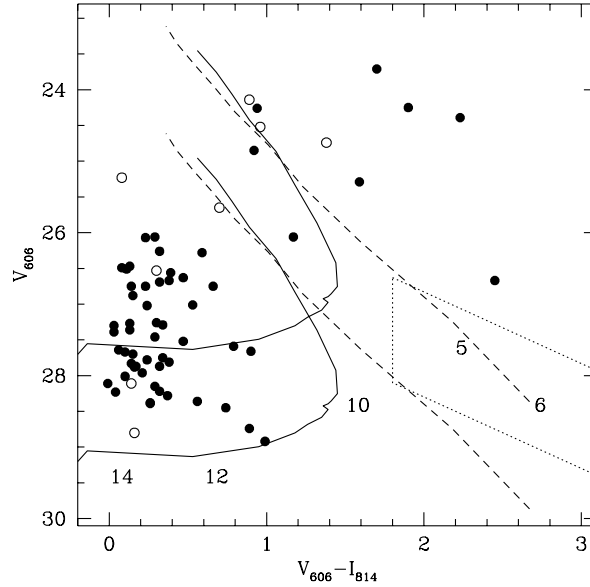


Fig. 2.— A color-magnitude diagram of Hubble Deep Field objects. The curves at the bottom left show the expected positions of white dwarf stars on the diagram. The points are candidate white dwarf stars that the HST barely detected in the deepest exposure ever taken. A 20-30-meter telescope with high-order optical adaptive optics correction could detect these objects and fainter ones easily in fewer than 10^4 seconds (see Tables 4 and 5).

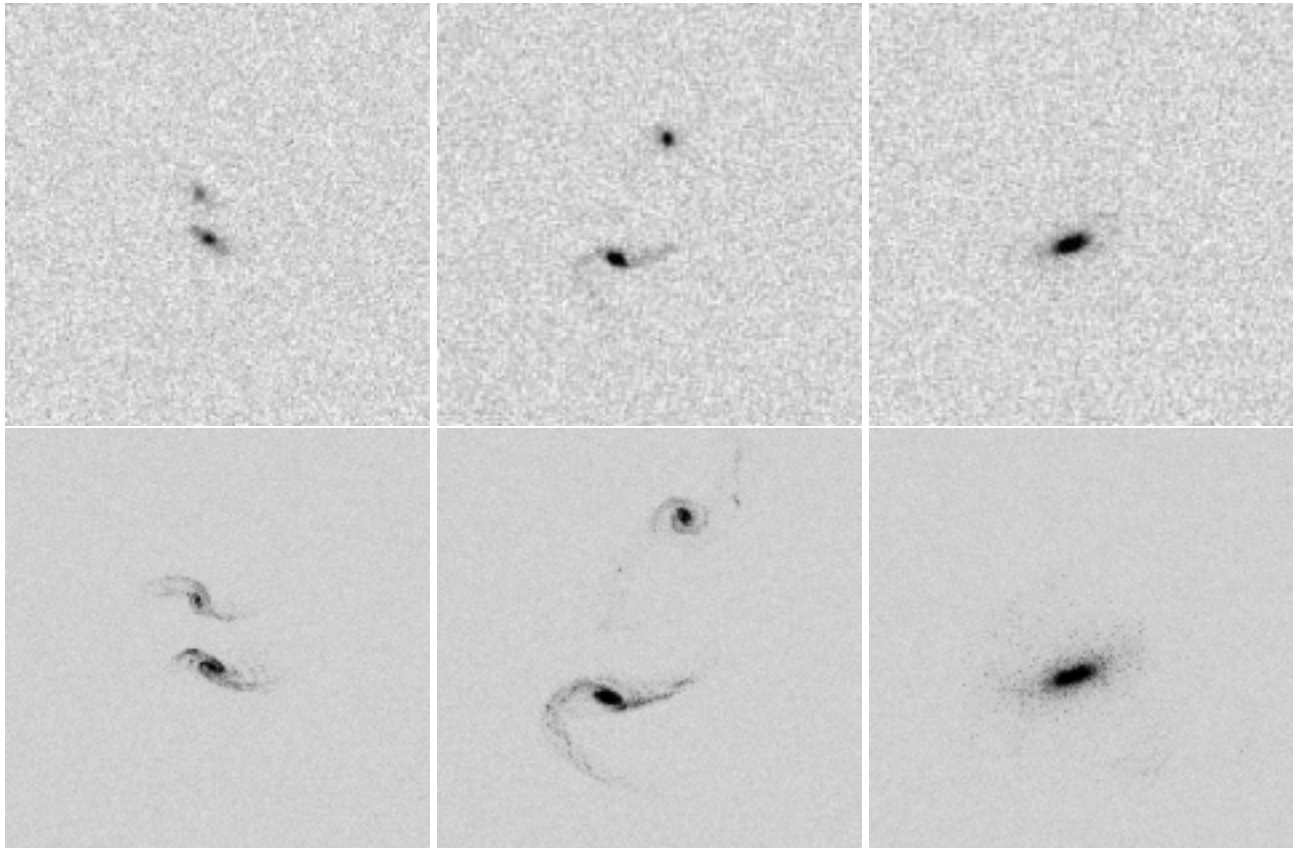


Fig. 3.— A simulated 2-hour visual exposure of a very distant pair of interacting galaxies, followed from $z=0.8$ (*far left*) to $z=0.6$ (*far right*) as the pair evolves: (*top*) with CFHT, and (*bottom*) as observed through a 20-meter XLT with nearly the theoretically best image quality possible (twice the diffraction limit).

corresponding to a dispersion of ~ 300 km/s. These data are only the tip of the iceberg of the high redshift Universe. They do not probe down to the star formation rates of the normal star-forming population at those redshifts. Moreover, the spectral resolution is too low to determine galaxy masses or the masses of the proto-groups and clusters which they presumably inhabit. Thus we have little information about the environment, masses or clustering properties of the bulk of star-forming galaxies at $z = 3$. In contrast, at low redshifts, by 2005, we will have a rich understanding of the large-scale clustering and dynamics and kinematics of representative volumes of the Universe via the 2dF redshift survey (250,000 galaxies) and Sloan Digital Sky Surveys (1 million galaxies) over scales of 100s of megaparsecs. Our goal in 2010 should be to have a view of the high-redshift Universe of comparable richness.

5.2. Goals

1. Measurement of power spectrum in linear regime and redshift-space and Alcock-Paczynski geometry distortion as a probe of geometry and biasing.
2. Identification of groups and proto-cluster environments in an objective and complete fashion.
3. Internal kinematics and hence masses (for brighter galaxies) from stellar absorption features; winds from interstellar features.
4. Relative kinematics of proto-galactic blobs to measure masses of the galaxies and their dark matter haloes in process of assembly.

5.3. Survey Parameters

With a 30 meter telescope, it should be possible to achieve $S/N=10$ spectra (per 3.4 Angstrom resolution element) down to a magnitude of $R_{AB} = 25.6$ in a 10000s exposure in 0.5 arcsec seeing (see Fig. 4 and Sec. 8.3). The resolution is sufficient to resolve a rest-frame velocity dispersion of 100 km/s. Thus one could obtain accurate redshifts *as well as* internal kinematic information for galaxies about a magnitude deeper than Steidel’s limit, and 1.2 magnitudes below L_* at that redshift. For redshift information alone ($S/N=3$) one could reach down to $R_{AB}=27$, two magnitudes below the Keck limit. The gain over Keck comes from the aperture as well as from the improved seeing. At a nominal depth of $R_{AB} = 26.5$, one is reaching 2 magnitudes below L_* , thus observing typical $z = 3$ galaxies as well as the bulk of the star-forming population in the Universe at that epoch. The areal density is approximately 4.2 galaxies per square arcmin.

With the Oke & Morbey (2001, PASP) spectrograph on a 20 meter, the field of view is 42 arcmin in diameter, with 1700 slits, but the central 36% of the area is obscured so the areal density of slits is 1.9 per square arcminute. Allowing for the dispersion and the fact that roughly half of the remaining field is vignetted, three 6.25 hour exposures are required to cover the unobscured field down to $R_{AB} = 26.5$. A square of 300 comoving h^{-1} Mpc has an area of 3.75 square degrees. This would require approximately 60 fields or 200 nights, and would yield 270,000 galaxy spectra, comparable to the 2dF and SDSS at $z = 0$.

With a 30m F/15 telescope and Oke-Morbey spectrograph, the exposures are reduced by 4/9 but the field size (20 arcmin) and the number of slits (1000) are less than in the 20m case. For this configuration, we estimate 150 nights for the same programme.

6. The Evolution of Galaxies

As described in Sec. 5, deep surveys with XLTs can detect and catalogue very distant galaxies at early stages in their evolutionary histories, the precursors to present-day galaxies. Imaging

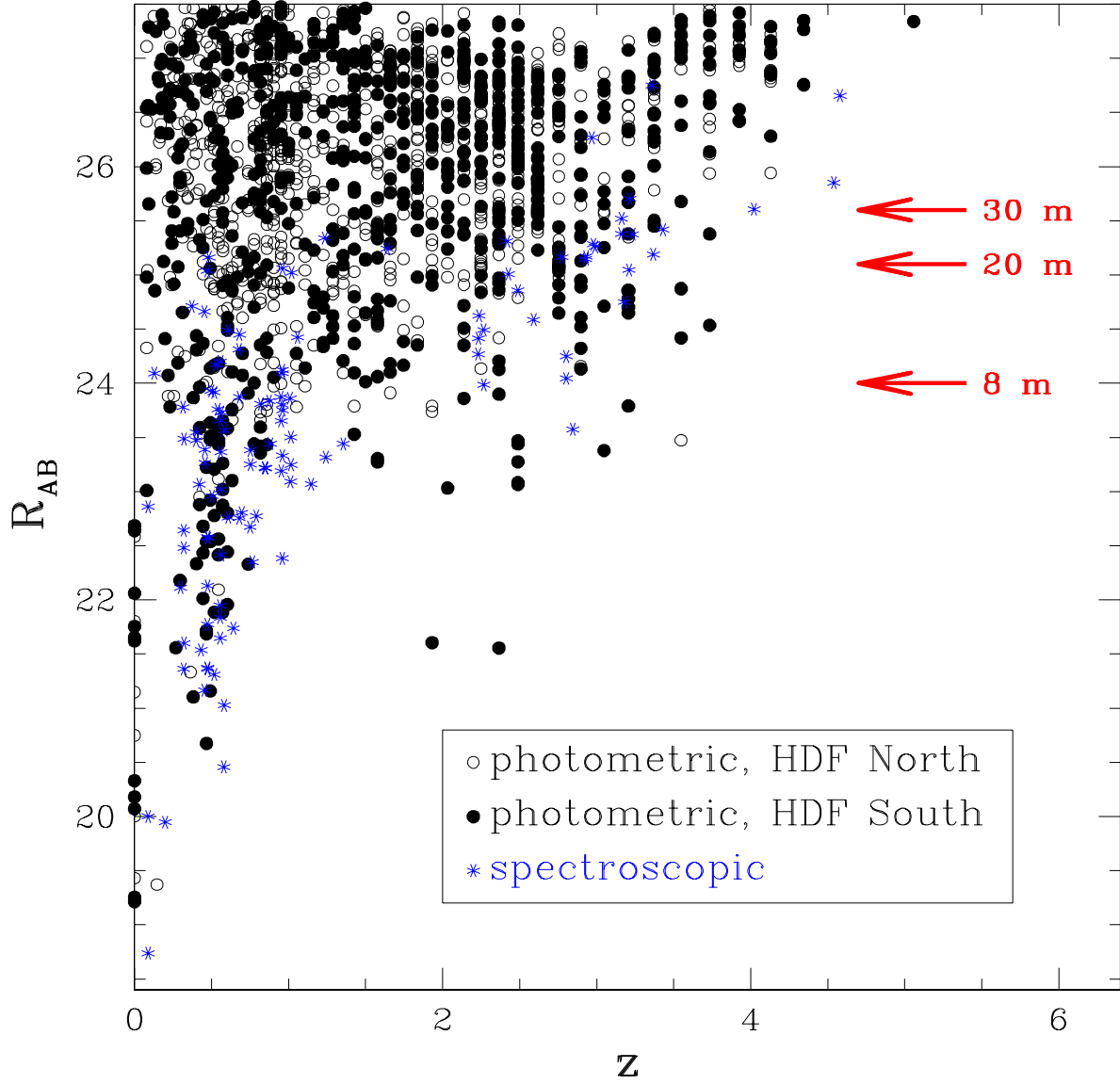


Fig. 4.— Galaxy counts from the Hubble deep fields (North and South). We plot the photometric or spectroscopic redshifts of HDF objects as a function of magnitude. The arrows show the flux limits for high-quality ($S/N = 10$) spectra with a 20 or 30-meter telescope in 10,000 seconds. Detection thresholds ($S/N = 3$) are ~ 1.4 magnitudes fainter for the same exposure time.

surveys (Sec. 4) reveal the unusual shapes of the objects. But more detailed knowledge, gained from further observations, may be required to understand their intrinsic properties.

Scaling laws for local galaxies show that the chemical compositions and internal kinematics of galaxies can reveal these intrinsic properties of objects. Measurements of the chemical abundances and the internal dynamics of very distant galaxies require the sensitivity and image quality available from 20 to 30-meter telescopes with adaptive optics.

6.1. Chemical Evolution of Galaxies

Concentrated bursts of star formation can lower the mass-to-light ratio of a galaxy and cause it to appear more optically compact than its true mass distribution. Thus, the total luminosities and sizes of galaxies may be poor indicators of their intrinsic properties. Chemical abundances can help resolve the degeneracies at intermediate redshift (e.g., Carollo & Lilly 2001, ApJ, 548, 153). Fig. 5 shows the accessibility of several important spectral features for studies of this kind as a function of redshift in the optical and near-IR. An XLT would be 1 to 2 magnitudes more sensitive than the current generation of large telescopes, allowing us to probe early objects much further down the luminosity function.

6.2. Internal Kinematics at Intermediate Redshift

The Tully-Fisher luminosity-linewidth relationship provides a basis for the direct detection of luminosity evolution in spiral galaxies. Galaxies of different ages that have the same rotation velocities can be compared directly. The differences in luminosities are a direct measure of the amount of the luminosity evolution of massive spirals from one epoch to another.

With existing telescopes and spectrographs, we measure the rotation speeds of only the brightest spiral distant galaxies, to $z \lesssim 1.2$. These observations require large amounts of telescope time. Furthermore, they are plagued by the possibility of systematic errors from the necessity of modeling the spatial distribution of the emission-line gas. Figs. 6 and 7 show how 20 to 30-meter XLTs with good near-IR image quality could survey *typical* spirals with relatively faint emission lines in the well-understood $H\alpha$ line to redshifts of ≥ 1.5 , with nearly as much spatial detail as present-day galaxies are studied today. A large sample of these observations, taken with a multi-IFU spectrograph, would provide a direct measure of the star formation history of spiral galaxies as a function of cosmic time.

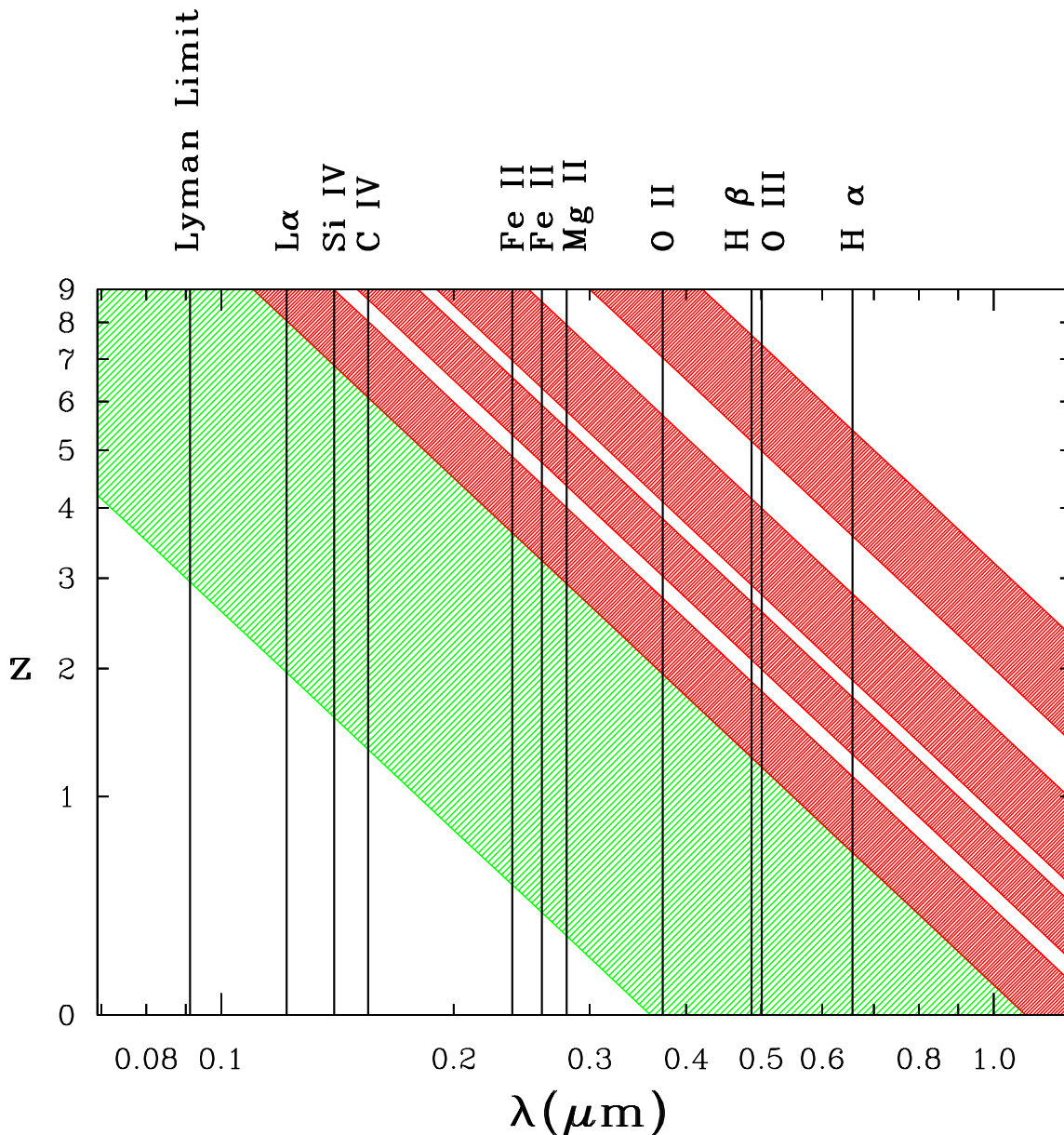


Fig. 5.— Spectral regions which can be observed from the ground as a function of redshift. These regions for redshift zero are shown at the bottom of the diagram. The domains for high redshift are at the top. The observable spectral bands in the objects shift to the left as the redshift increases. The lightly shaded region highlights the features observable with the proposed visible-light spectrograph. A near-infrared spectrograph could see the darker regions. Sec. 8.3 discusses the spectroscopic sensitivity of a multi-object spectrograph on an XLT.

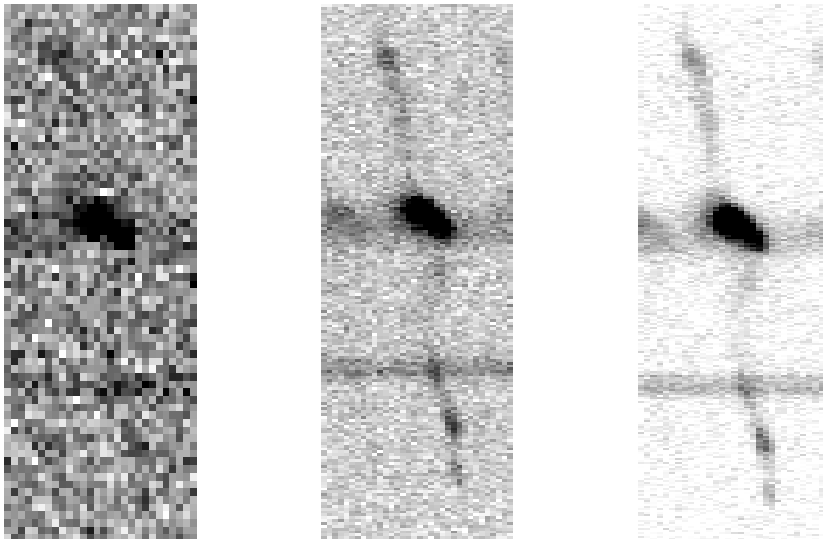


Fig. 6.— An artificially-redshifted longslit spectrum of a spiral galaxy with $M_B = -21.7$ at $z = 1$, as seen in the $H\alpha$ line (near-IR), through an 8-meter (left), 20-meter (middle) or 30-meter (right) telescope. We redshift an optical $H\alpha$ spectrum, assuming a 10-hour observation through an efficient spectrograph with very good image quality (J-band Strehl of 0.7).

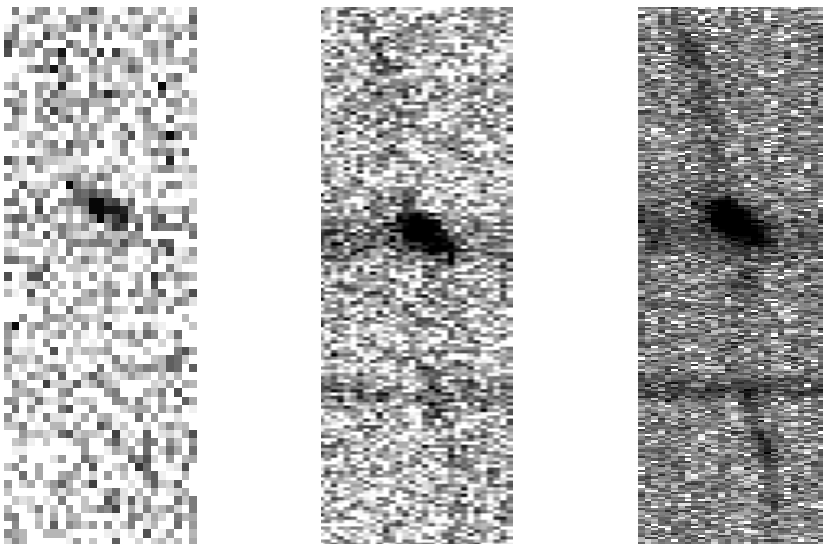


Fig. 7.— An artificially-redshifted longslit spectrum of the same nearby spiral galaxy at $z = 1.5$, also in the $H\alpha$ line but with a 20-hour exposure, through an 8-meter (left), 20-meter (middle) or 30-meter (right) telescope. The H-band Strehl ratio we assume is 0.82. Only the central emission is evident in the 8-meter data. The faint emission in the outskirts of the galaxy is visible through the 20 meter and, especially, the 30 meter, and the rotation curve could be extracted with careful data analysis.

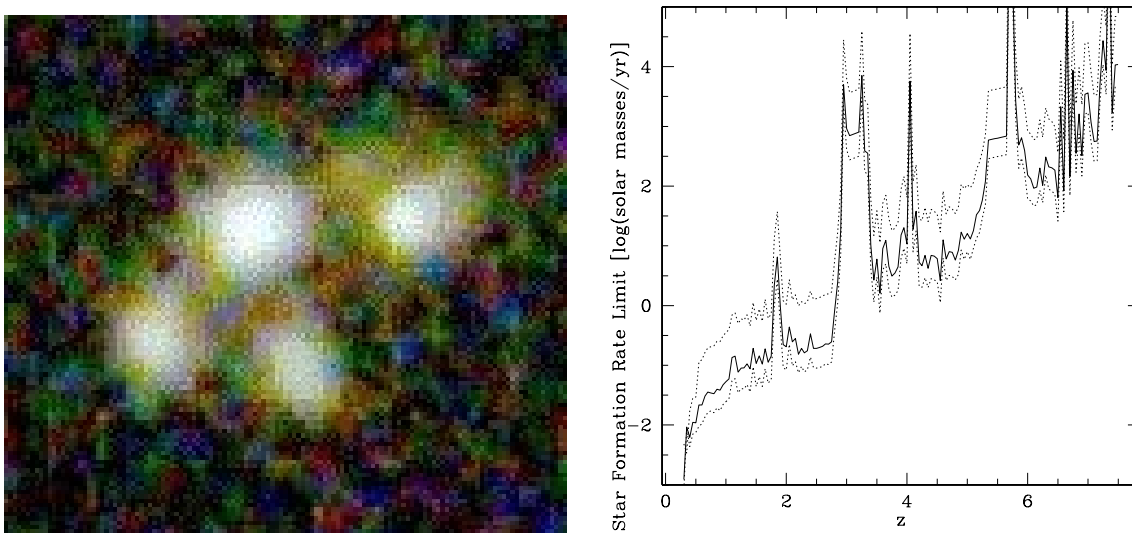


Fig. 8.— (left) An example of a “Lyman break” galaxy in the Hubble deep field. These four lumps may be four galaxies merging together or four star-forming regions inside the same galaxy. A 20 to 30-meter telescope would enable us to distinguish between these possibilities for large samples of similar objects, using measurements of the relative velocities of these kinds of lumps. (right) The limiting star formation rate as a function of redshift in the $H\alpha$ line, for a S/N of 10 in 10^4 seconds with an 8-meter (top, dotted), 20-meter (middle, solid), or 30-meter (bottom, dotted) telescope. See Sec. 8.5 for details of the calculation.

6.3. Very Distant and Young Objects: “Lyman Break” Galaxies and Beyond

Recent studies of very distant objects reveal a population of galaxies at a redshifts of 3 to 4. The “Lyman break” galaxies are a varied population of objects, with star formation rates of $\sim 100 \text{ M}_{\odot} \text{ yr}^{-1}$. Some appear round, others are amorphous or lumpy like the object in Fig. 8a. The nature of Lyman break galaxies is heavily debated. They may be intrinsically large galaxies or smaller galaxies that are very luminous due to recent star formation. In some cases, measurements of the internal motions of the galaxies could resolve this degeneracy. For most Lyman break galaxies, these measurements require both the sensitivity and the resolving power of large-aperture telescopes.

Fig. 8b shows the sensitivity of an IFU on an XLT to unresolved star formation in the $\text{H}\alpha$ line as a function of redshift. If the lumps of star formation are very centrally concentrated, measurements of the internal motions in Lyman break galaxies are possible with a 20 or 30-meter telescope. If the image quality is near the diffraction limit in the near-infrared, a 20-meter telescope could measure the velocity of an unresolved lump of star formation with a very low star-formation rate in 3 hours (0.1 solar masses per year of $\text{H}\alpha$ flux at a redshift of about 3). A 30-meter telescope could measure the velocity of a lump with $\sim 50\%$ of this flux. For lumpy, concentrated objects with very high star formation rates, velocities could be measured at much higher redshifts.

6.4. The First Star Formation in the Universe

The earliest star-forming objects in the Universe may have strong $\text{Ly}\alpha$ emission (e.g., Miralda-Escudé & Rees 1998, ApJ, 497, 21). Fig. 9 shows the sensitivity of an IFU to line flux from an unresolved point source (see Sec. 8.5 for details). An IFU-based survey for the earliest star formation would probe many magnitudes deeper than existing surveys (e.g., Rhoads et al. 2000, ApJ, 545, 85, which focused on targets in the range of $2.6 - 5.2 \times 10^{-17} \text{ ergs cm}^{-2} \text{ s}^{-1}$).

7. High-resolution Stellar Spectroscopy

High spectral resolution is necessary to distinguish the often weak and blended features found in the spectra of stars, quasars, and the interstellar medium. These features indicate the detailed composition, temperature, velocity, and/or other properties of the target object, some of which cannot be determined any other way.

These spectra, however, come at a high cost. Because the light is broken up into so many pieces, each gets very little light. As the example in the figure shows, even the largest telescopes today place limits on the type of science that can be done at high resolution. This is especially true for the blue and near-UV, where many of important spectral features lie. A 30-meter telescope with a high resolution spectrograph would greatly benefit research at these wavelengths.

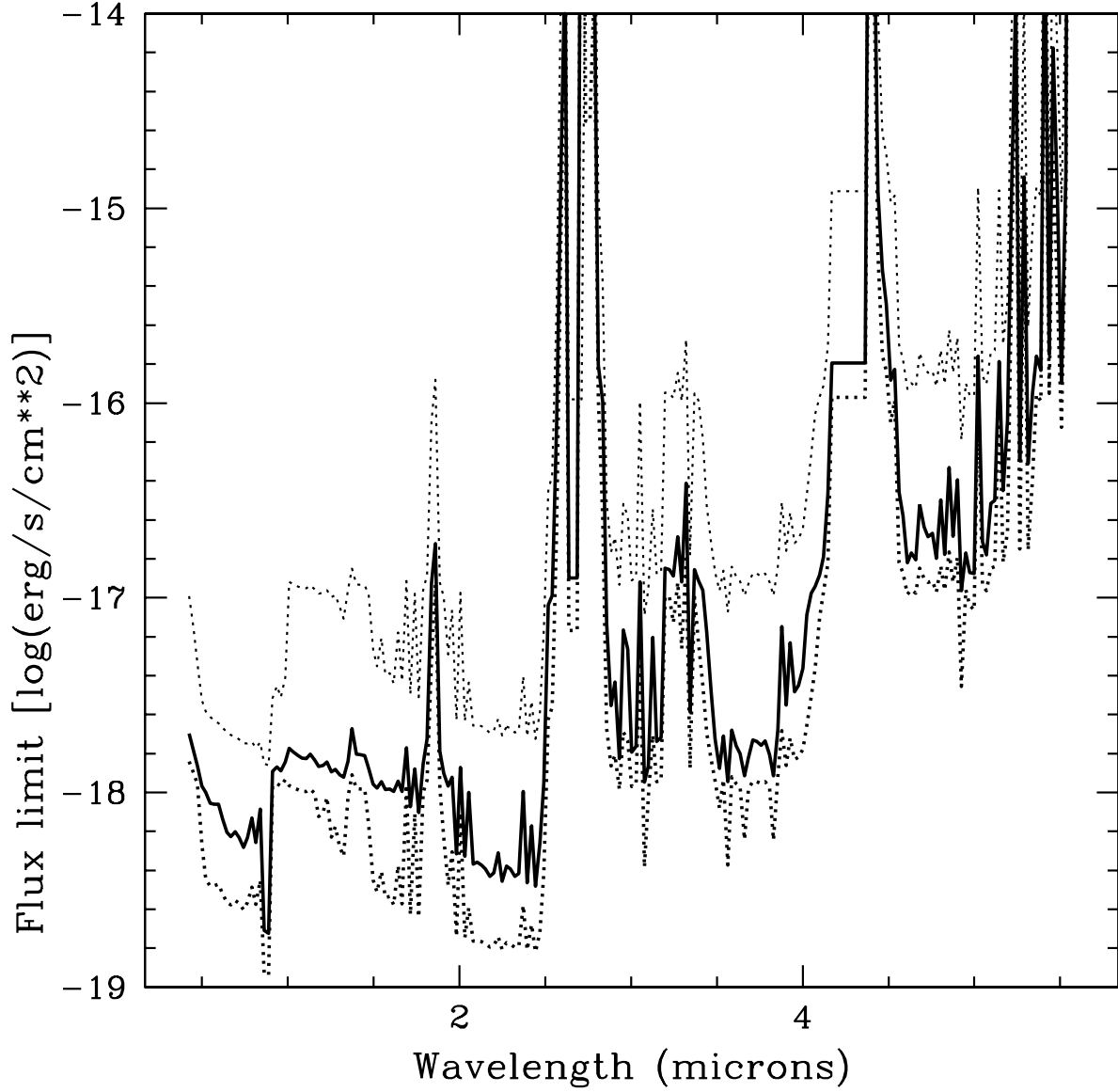


Fig. 9.— Unresolved-source sensitivity limits for an IFU in the “expected” AO performance case. The jagged lines show limiting line fluxes ($S/N=10$) in 10^4 seconds, for an 8-meter (dotted; top), 20-meter (solid; middle) and 30-meter (dotted; bottom) aperture, with $R=3000$. See Table 13 for parameters of the S/N calculation.

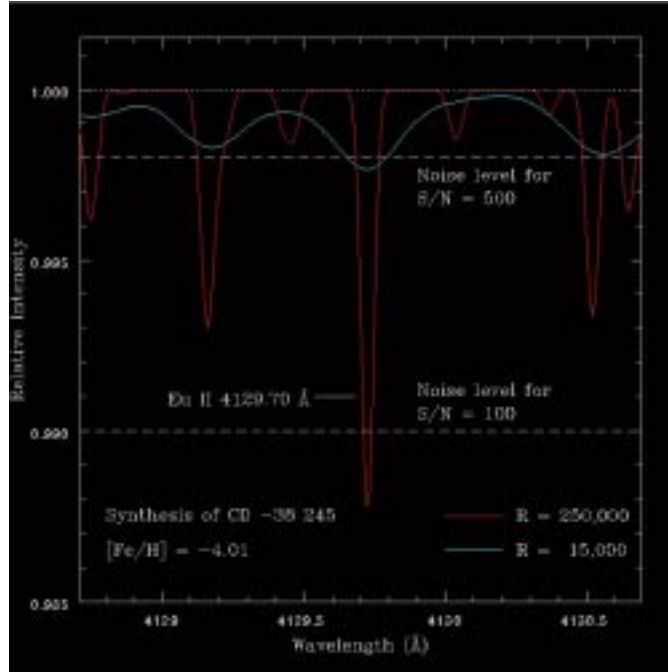


Fig. 10.— One application of high-resolution spectroscopy: the abundance analysis of stars, key to understanding the origins of the chemical elements and the early formation of our Galaxy. The colored lines are a noiseless simulated spectrum of CD -38 245, the most metal-poor star known—a fossil record of the earliest material the Galaxy. One important diagnostic is the r-process element Europium (Eu); its strongest spectral line plotted here. In this star, the line is too weak to show contrast at moderate resolution (blue), but stands out at higher resolution (red). However, for even this relatively bright star ($m_V = 12$), the necessary signal requires a full-night exposure on a 10-m class telescope. This makes it unreasonable to obtain the sample sizes necessary to understand the chemical evolution of the Galaxy. However, on, e.g., a 30-m telescope, the same observation would take about an hour, allowing a comprehensive study of this important population.

The design and construction costs of a high-resolution spectrograph for a 30-meter telescope can be kept comparable to those of modern instruments (UVES on the VLT, HIRES on Keck I) if the telescope has high quality natural seeing. Such a system would not need adaptive optics and would yield a resolution (R) of about 50,000. Another, more challenging, design would allow resolutions of nearly 250,000 with image slicers and could work at lower resolutions without a slicer in order to allow accurate sky subtraction. It is likely that natural technological advancements will make such a design feasible by the time a 30-meter telescope is in advanced development.

8. Performance Calculations

Differing assumptions about detectors, telescopes, background, and sources present serious problems for comparing and evaluating claims of expected telescope performance. In this section, we present performance calculations along with the assumptions we use. Table 2 lists the definitions of various relevant parameters. For each sensitivity calculation, we include a separate table of the values we assume for these parameters.

Because the expected background at L2 is extremely low, the detector performance determines the sensitivity of NGST (and ground-based instruments) in low-photon regimes. For a fair comparison to NGST, we use the NGST Requirements as our detector parameters.

8.1. Formulas for Signal-to-Noise Calculations

Here, we present the basic equations used for signal-to-noise calculations in this Section.

Spatial pixel size for appropriate sampling:

$$\theta_{\text{pix}} = \theta_s/2 \quad (1)$$

Number of exposures:

$$N_{\text{exp}} = \frac{\text{signal} + \text{noise}}{W_{e^-}} \quad (2)$$

Readnoise:

$$\text{readnoise} = R_{e^-}^2 N_{\text{exp}} N_{\text{pix}} \quad (3)$$

Dark current (electrons):

$$\text{dark current} = N_{\text{pix}} (DK_{e^-}) T \quad (4)$$

Sky measurement noise (electrons):

$$\text{sky measurement noise} = \text{sky noise} \left(\frac{1}{\sqrt{N_{\text{sky}}}} \right) \quad (5)$$

Table 2. Definitions of Parameters in S/N Calculations

Quantity	Description
Telescope + Instrument	
D	Diameter of primary mirror
f_{mirror}	Filling factor of mirror
ϵ	Total efficiency (telescope+instrument+detector)
Detector	
R_{e^-}	Readnoise (RMS, electrons)
(DK_{e^-})	Dark current (electrons)
W_{e^-}	Detector well capacity, electrons
$\theta_{\text{pix},s}$	Pixel size (spatial units, arcsec)
θ_{slit}	Aperture width for 1-D (longslit) spectroscopy
Ω_{element}	Solid angle of element for 2-D spectroscopy
Observation	
T	Total integration time
$(\Delta\lambda)$	Width of filter or resolution element
X	Airmass
(ext)	Extinction (magnitudes per airmass)
f_{sky}	Sky counts*, photons/cm ² /Å/s/□''
N_{exp}	Number of exposures
f_0	Photometric zero point, erg/cm ² /Å/s
θ_s	Image FWHM
Data Reduction	
N_{pix}	Number of pixels used for detection/measurement
$N_{\text{pix},s}$	Number of pixels extracted along slit (for 1-D spectroscopy)
f_{pix}	Fraction of light from the source on these pixels
N_{sky}	(Area used for sky measurement)/(Area of extracted observations)

*Includes sky and telescope background; at present, there is no scattered light term.

Signal-to-Noise Ratio (per λ resolution element):

$$\text{SNR} = \frac{\text{signal}}{\sqrt{\text{signal} + (1 + \frac{1}{N_{\text{sky}}}) (\text{readnoise} + \text{dark current} + \text{sky})}} \quad (6)$$

Object photon flux:

Per arcsecond, from surface brightness:

$$f_{\text{obj,ang}} = f_0 \cdot 10^{[-0.4(\mu + (\text{ext})X)]} \frac{\lambda}{hc} \quad (7)$$

Total, from magnitude:

$$f_{\text{obj}} = f_0 \cdot 10^{[-0.4(m + (\text{ext})X)]} \frac{\lambda}{hc} \quad (8)$$

8.1.1. Imaging

Sky counts (electrons):

$$\text{sky} = \epsilon \cdot f_{\text{sky}} \pi f_{\text{mirror}} \left(\frac{D}{2} \right)^2 (\Delta\lambda) T N_{\text{pix}} \theta_{\text{pix,s}}^2 \quad (9)$$

Signal (electrons):

$$\text{signal} = \epsilon \cdot f_{\text{pix}} f_{\text{obj}} \pi f_{\text{mirror}} \left(\frac{D}{2} \right)^2 (\Delta\lambda) T N_{\text{pix}} \theta_{\text{pix,s}}^2 \quad (10)$$

8.1.2. One-Dimensional Spectroscopy

Sky counts (electrons):

$$\text{sky} = \epsilon \cdot f_{\text{sky}} \pi f_{\text{mirror}} \left(\frac{D}{2} \right)^2 (\Delta\lambda) T \theta_{\text{slit}} N_{\text{pix,s}} \theta_{\text{pix,s}} \quad (11)$$

Object counts (electrons):

$$\text{signal} = \epsilon \cdot f_{\text{pix}} f_{\text{obj}} \pi f_{\text{mirror}} \left(\frac{D}{2} \right)^2 (\Delta\lambda) T \theta_{\text{slit}} N_{\text{pix,s}} \theta_{\text{pix,s}} \quad (12)$$

8.1.3. Two-Dimensional Spectroscopy

Sky counts (electrons):

$$\text{sky} = \epsilon \, f_{\text{sky}} \pi f_{\text{mirror}} \left(\frac{D}{2} \right)^2 (\Delta\lambda) T \Omega_{\text{element}} \quad (13)$$

Object counts (electrons):

$$\text{object} = \epsilon \, f_{\text{pix}} f_{\text{obj}} \pi f_{\text{mirror}} \left(\frac{D}{2} \right)^2 (\Delta\lambda) T \Omega_{\text{element}} \quad (14)$$

8.2. Sensitivity of a Broad-band Imager to Point Sources

Tables 3 – 5 list point-source sensitivity estimates for 10^4 seconds, to a signal-to-noise ratio (S/N) of 10. We include read noise, dark current (near-IR only), sky noise, and sky subtraction error. The tables list sensitivities in optical and near-infrared bands (R=5) for telescopes with various aperture sizes under three separate assumptions about the image quality. The range of assumptions are intended to bracket the image-quality possibilities for real telescopes.

The first table describes the point-source sensitivity in the estimated median seeing conditions (0."5 at V, 0."4 at K). The second and third tables describe “expected” and “optimistic” adaptive optics (AO) system performance, using an empirically-motivated prescription for the AO psf. The psf consists of two Gaussians: a central “core” and “wings”. In the approximation, the Strehl ratio is the ratio of fluxes in the two Gaussians. In both cases, the wings have a FWHM of 70% of the natural seeing and the core has a diffraction-limited FWHM, except in the “expected” case for the optical bands, where the core is 50% of the natural seeing. Fig. 11 shows the image quality as a function of wavelength for the two cases, respectively. Table 6 details these assumptions.

Table 3. Limiting Magnitudes for Point Sources in 10^4 Seconds to S/N=10 in Natural Seeing^a

Aperture	<i>U</i>	<i>B</i>	<i>V</i>	<i>R</i>	<i>I</i>	<i>J</i>	<i>H</i>	<i>K</i>
8 meter	26.7	27.8	27.4	26.8	26.4	24.3	23.1	22.7
20 meter	27.7	28.8	28.4	27.8	27.4	25.3	24.1	23.7
30 meter	28.2	29.2	28.8	28.3	27.8	25.7	24.5	24.1

^a0".5 at V, ".4 at K.

Table 4. Limiting Magnitudes for Point Sources in 10^4 Seconds to S/N=10, Expected AO Performance^{a,b}

Aperture	<i>U</i>	<i>B</i>	<i>V</i>	<i>R</i>	<i>I</i>	<i>J</i>	<i>H</i>	<i>K</i>
8 meter	27.2	28.2	27.8	27.3	26.9	25.7	24.7	24.3
20 meter	28.1	29.2	28.8	28.3	27.9	27.6	26.6	26.2
30 meter	28.6	29.6	29.2	28.7	28.3	28.5	27.5	27.1

^aStrehl of 0.05 at V, 0.7 at K.

^bSee Sec. 8.1 for the relevant calculations and Table 6 for a list of assumptions.

Table 5. Limiting Magnitudes for Point Sources in 10^4 Seconds to S/N=10, Optimistic AO Performance^{a,b}

Aperture	<i>U</i>	<i>B</i>	<i>V</i>	<i>R</i>	<i>I</i>	<i>J</i>	<i>H</i>	<i>K</i>
8 meter	28.4	29.5	29.2	28.7	28.3	26.1	25.0	24.5
20 meter	30.4	31.5	31.2	30.7	30.3	28.1	27.0	26.5
30 meter	31.3	32.4	32.0	31.6	31.2	29.0	27.9	27.4

^aStrehl of 0.2 at V, 0.9 at K.

^bSee Sec. 8.1 for the relevant calculations and Table 6 for a list of assumptions.

Table 6. Assumptions for Point-Source Sensitivity Calculations

Parameter	Value
D	8, 20, 30 meters
f_{mirror}	0.9
ϵ (optical)	0.5
ϵ (near-IR)	0.4
R_{e-} (optical)	$4 e^-$
R_{e-} (near-IR)	$15 e^-$
(DK_{e-}) (optical)	0
(DK_{e-}) (near-IR)	$0.02 e^- s^{-1} \text{ pixel}^{-1}$
W_{e-} (optical)	$9 \times 10^4 e^-$
W_{e-} (near-IR)	$6 \times 10^4 e^-$
$\theta_{\text{pix},s}$	half of core FWHM (see below) in V (optical) or K (near-IR)
T	10^4 seconds
$(\Delta\lambda)$	$\lambda_0/5$ (R=5)
X	1.0 airmass
Sky/extinction	Mauna Kea
θ_s (natural seeing)	0."5 at V, 0."4 at K
θ_s ("core", expected AO)	$0.5 \times$ natural seeing, at V diffraction limit, near-IR
θ_s ("core", optimistic AO)	diffraction limit
θ_s ("wings", any AO)	$0.7 \times$ natural seeing
Strehl (expected AO)	0.05 in V, 0.7 in K
Strehl (optimistic AO)	0.2 in V, 0.9 in K
N_{pix}	Optimized (square aperture)
N_{sky}	9

8.3. Sensitivity of a Natural Seeing Multi-object Spectrograph

Table 7 lists limiting magnitudes for a wide-field multi-object spectrograph used in natural seeing (0."3 or 0."5). Fig. 12 shows these limits as a function of wavelength. We detail the assumptions in Table 8. The optical magnitudes are appropriate for the spectrograph design in Sec. 9. Because the sky spectrum was not smoothed, the results assume some OH suppression.

8.4. Sensitivity of a Natural Seeing High-resolution Spectrograph

Table 9 lists limiting magnitudes for a high-resolution spectrograph used in “median” natural seeing (0."5), for $S/N = 10$ and $S/N = 1000$ observations. We detail the assumptions in Table 10. The calculations are similar to Sec. 8.3, with a spectrograph 50% as efficient as its lower-resolution counterpart.

8.5. Sensitivity of an Integral Field Unit Spectrograph with Adaptive Optics

Fig. 9 and Tables 11 and 12 show IFU sensitivity estimates for 10^4 seconds, to a signal-to-noise ratio (S/N) of 10. As in Sec. 8.2, the tables list sensitivities in optical and near-infrared bands ($R=3000$) for telescopes with various aperture sizes. We use “expected quality” assumptions about the adaptive optics correction; the results are relatively insensitive to these assumptions. We list assumptions in Table 13.

9. Instrumentation: A Low-Resolution Multi-Slit Spectrograph for 20-30 Meter Telescopes

In this section, a design is proposed for a slitmask spectrograph for a three-mirror wide-field 20-metre telescope that overcomes the problem of the very large physical size of the focal surface. An almost identical design can also be applied to a 30-metre Cassegrain telescope. The design divides the focal surface into many spectrograph cells which are deployed in a hexagon pattern to cover the field of view. When fully implemented, in a single exposure one can obtain up to 1700 spectra in the 20-metre telescope design and 1030 spectra in the 30-metre design. The weight of the fully implemented instrument is approximately 16,500 kg and the the cost is approximately US\$18,000,000.

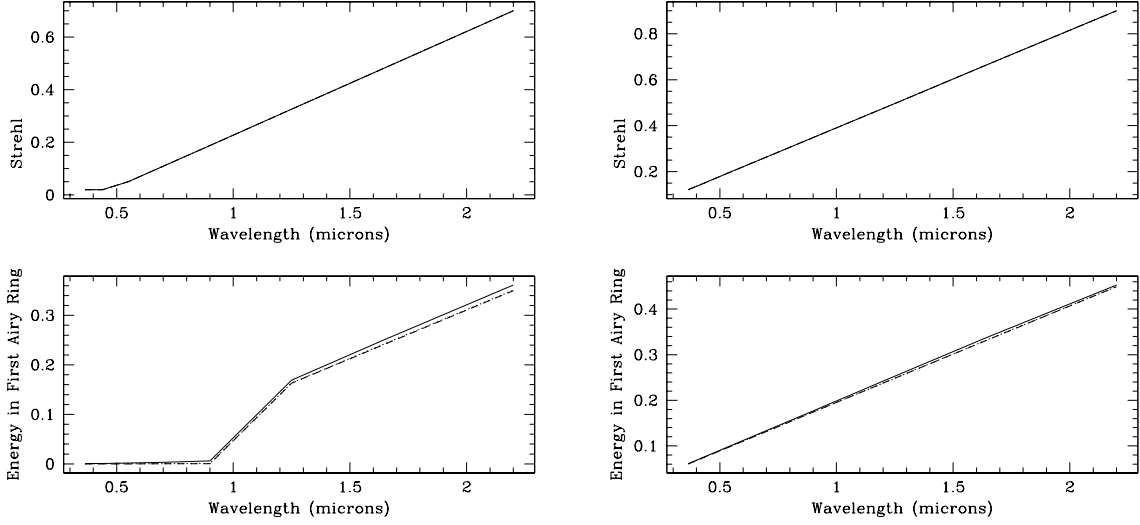


Fig. 11.— Image quality in the “expected” (left) and “optimistic” (right) AO performance cases. The top panels show the Strehl ratio as a function of wavelength; the bottom panels shows the energy contained in the first Airy ring, for an 8-meter (solid), 20-meter (dotted) and 30-meter (dashed) telescope. The encircled energy is 50% for a single Gaussian.

Table 7. Sensitivity Estimates for Continuum Spectra, $S/N = 10^a$ in 10^4 seconds

Telescope Aperture	0."3 seeing			0."5 seeing		
	R_{AB} limit ^b	I_{AB} limit ^c	K_{AB} limit ^d	R_{AB} limit	I_{AB} limit	K_{AB} limit
8m	24.4	24.1	22.1	24.0	23.6	21.8
20m	25.6	25.2	23.5	25.1	24.7	23.0
30m	26.1	25.7	24.0	25.6	25.1	23.4

^aLimits for $S/N=3$ are ~ 1.3 magnitudes fainter.

^bat 6400 Å

^cat 8200 Å

^dat 22100 Å

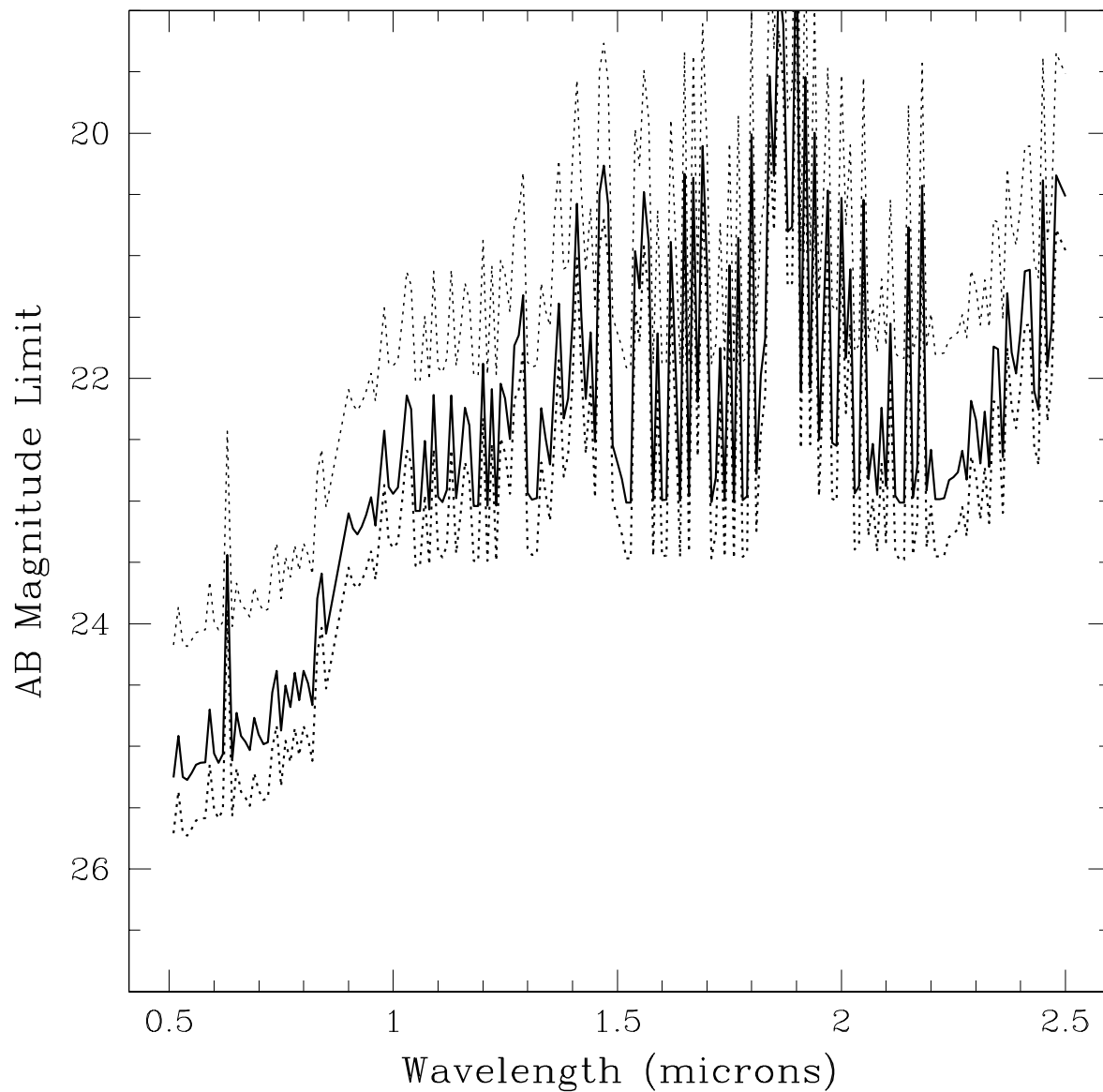


Fig. 12.— Sensitivity of a natural-seeing ($0.''5$) multi-object spectrograph as a function of wavelength. We show the limiting magnitudes for a S/N of 10 per 3.4 \AA resolution element with an 8-meter (dotted, top), 20-meter (solid, middle), and a 30-meter (dotted, bottom) telescope.

Table 8. Assumptions for the Multi-object Spectrograph Sensitivity Estimates

Parameter	Value
f_{mirror}	0.9
ϵ (optical)	0.33
ϵ (IR)	0.26
Readnoise (optical)	4 e^-
Readnoise (IR)	15 e^-
(DK $_{e^-}$) (optical)	0
(DK $_{e^-}$) (IR)	0.02 $e^- \text{ s}^{-1} \text{ pixel}^{-1}$
W_{e^-} (optical)	$9 \times 10^4 e^-$
W_{e^-} (IR)	$6 \times 10^4 e^-$
θ_{slit}	$1.25 \times \text{seeing FWHM}$
T	10^4 seconds
$(\Delta\lambda)$	3.4 \AA
X	1.5 airmasses
Sky/extinction	Mauna Kea
θ_s	0.''3, 0.''5
N_{pix}	25
f_{pix}	0.78
N_{sky}	9

Table 9. Sensitivity Estimates for Continuum Spectra, 0.''5 seeing^a in 10^4 seconds

Telescope Aperture	S/N=10			S/N=1000		
	R_{AB} limit ^a	I_{AB} limit ^b	K_{AB} limit ^c	R_{AB} limit	I_{AB} limit	K_{AB} limit
8m	21.2	21.2	19.9	12.4	12.5	12.3
20m	22.9	22.7	21.5	14.4	14.4	14.2
30m	23.5	23.2	22.1	15.3	15.3	15.1

^aat 6400 \AA

^bat 8200 \AA

^cat 22100 \AA

Table 10. Assumptions for the High-resolution Spectrograph Sensitivity Estimates

Parameter	Value
f_{mirror}	0.9
ϵ (optical)	0.16
ϵ (IR)	0.13
Readnoise (optical)	4 e^-
Readnoise (IR)	15 e^-
(DK $_{e^-}$) (optical)	0
(DK $_{e^-}$) (IR)	0.02 $e^- \text{ s}^{-1} \text{ pixel}^{-1}$
W_{e^-} (optical)	$9 \times 10^4 e^-$
W_{e^-} (IR)	$6 \times 10^4 e^-$
θ_{slit}	$1.25 \times \text{seeing FWHM}$
T	10^4 seconds
$(\Delta\lambda)$	$\frac{\lambda}{30,000}$
X	1.5 airmasses
Sky/extinction	Mauna Kea
θ_s	0.''3, 0.''5
N_{pix}	25
f_{pix}	0.78
N_{sky}	9

Table 11. Emission-line Flux Sensitivities for an IFU^a

Aperture	Limiting line flux [$\log(\text{erg/s/cm}^2)$]					
	$\lambda = 5000\text{\AA}$	$\lambda = 7000\text{\AA}$	$\lambda = 1.1\mu\text{m}$	$\lambda = 1.6\mu\text{m}$	$\lambda = 2.2\mu\text{m}$	$\lambda = 3.5\mu\text{m}$
8 m	-17.5	-17.7	-16.9	-17.4	-17.6	-16.9
20 m	-18.0	-18.2	-17.8	-18.0	-18.4	-17.7
30 m	-18.4	-18.6	-18.0	-18.6	-18.8	-18.0

^aLimiting fluxes to $S/N=10$ in 10^4 seconds. See Table 13.

9.1. Design Approach

A practical problem in the design of multiobject spectrographs for very large telescopes is that the optical components in the spectrograph become impossibly large. For example, a 20-metre telescope working at F/11 at the Cassegrain and having a 42 arcmin diameter field has a focal surface which is 2.67 metres in diameter.

One obvious way to overcome the enormous optics and complexity of a single spectrograph is to break the field up into a large number of smaller areas or cells and design a straight-through spectrograph for a single cell and then replicate it many times.

9.2. Straight-Through Spectrograph design

The aim in the spectrograph design is to enclose the whole spectrograph cell in a stainless steel tube with a diameter of 355.6 mm (14 inches). Our camera design is shown in Fig. 13. The telescope focal surface is at the left, the CCD mosaic detector at the right. The dispersion is provided by a grism with a 450 groove mm^{-1} grating and a 39 degree fused quartz prism. Assuming that we use current 2000 by 4000 pixel CCDs with 12.5μ pixels, we require a 2 by 2 mosaic to cover the field adequately. Typical images over the field of the CCD mosaic have diameters of 12-16 μ corresponding to $\sim 0.10''$ and are shown in Fig. 14. For a telescope image of 0.25 arcsec the spectrograph resolution is 3000 or 2Å.

Characteristics of the focal plane of the spectrograph are shown in Table 14.

The design for a 30-metre F/15 Cassegrain telescope would be almost identical and Table 14 would be only slightly changed.

At the CCD mosaic, the unvignetted field of view of 44.4 mm is shown by the circle in Fig. 15. Slits should be located within the area outlined by the inner rectangular box. Spectra going from 4000 to 9500Å are also shown in the figure. The layout of four-CCD mosaic is also shown.

9.3. The Array of Cells

Having designed the straight through individual spectrograph cells, they now must be replicated and arrayed over the full field of view of the telescope. One obvious mounting approach would be to stack the individual cells in a hexagonal pattern shown in Fig. 16. The outer circle is the full telescope field. The layout in the telescope focal surface for three adjacent cells in a hexagon pattern is shown in Fig. 17. The rectangles indicate where slits should be deployed. A single exposure can access half of the objects in the whole field. By shifting the telescope by about 0.5 cell diameters one can set on objects in the other half of the field.

For the 20-metre 3-mirror design, shown in Fig. 18, there is an area at the centre of the field

Table 12. Star Formation Rate Sensitivities

Aperture	Limiting H α Star Formation Rate ^a [log(M $_{\odot}$ yr $^{-1}$)]				Limiting OII Star Formation Rate [log(M $_{\odot}$ yr $^{-1}$)]			
	$z = 0.3$	$z = 1$	$z = 2$	$z = 4$	$z = 1.5$	$z = 2.5$	$z = 3.5$	$z = 5$
8 m	-2.3	-0.5	0.0	1.8	0.1	0.8	0.8	1.0
20 m	-2.9	-1.3	-0.7	1.0	-0.5	-0.1	0.3	0.2
30 m	-3.1	-1.6	-1.1	0.7	-0.6	-0.4	-0.3	-0.1

^aAssuming Kennicutt (1998) conversion from H α and [OII](3727Å) flux to star formation rate, with no internal extinction, $q_0 = 0.1$, $H_0 = 70$ km s $^{-1}$ Mpc $^{-1}$.

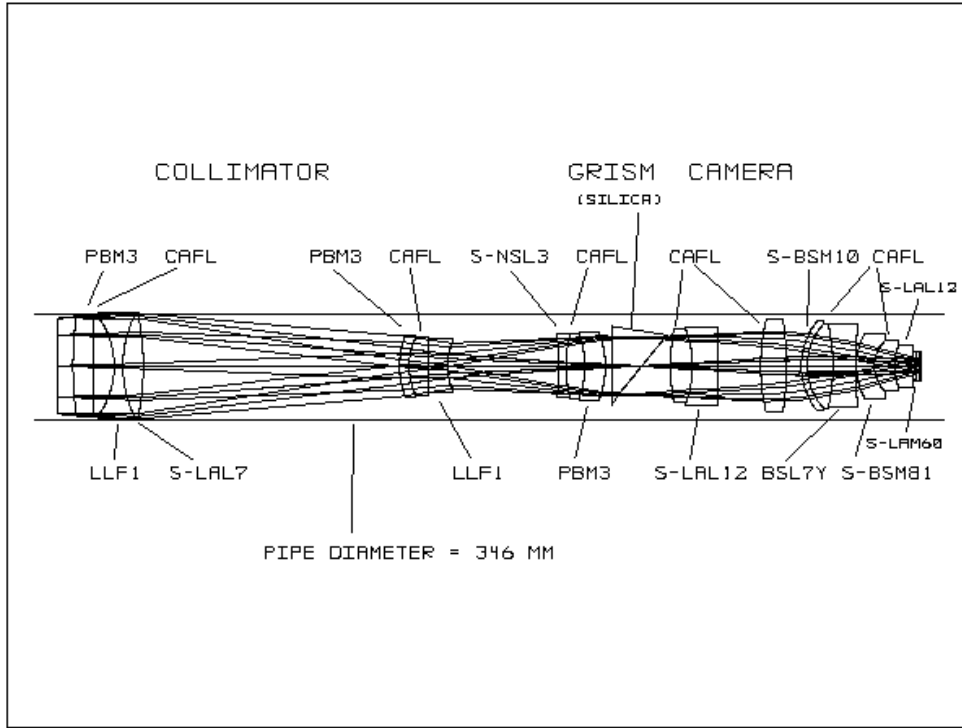


Fig. 13.— Optical design for a spectrograph cell for a 20-metre F/11 3-mirror telescope. The telescope focal plane is at the left and the detector is at the right. A telescope pupil is formed at the grism. All the optics fit inside a tube which is 355.6 mm in diameter and 2.67 metres long.

Table 13. Assumptions for the IFU Emission-Line Sensitivity Estimates

Parameter	Value
D	8, 20, 30 meters
f_{mirror}	0.9
ϵ (optical)	0.26
ϵ (near-IR)	0.21
R_{e-} (optical)	$4 e^-$
R_{e-} (near-IR)	$15 e^-$
(DK_{e-}) (optical)	0
(DK_{e-}) (near-IR)	$0.02 e^- s^{-1} \text{ pixel}^{-1}$
W_{e-} (optical)	$9 \times 10^4 e^-$
W_{e-} (near-IR)	$6 \times 10^4 e^-$
$\theta_{\text{pix},s}$	half of core FWHM (see below) in V (optical) or K (near-IR)
T	10^4 seconds
$(\Delta\lambda)$	$\frac{\lambda_0}{3000}$ (R = 3000)
X	1.5 airmasses
Sky/extinction	Mauna Kea
θ_s (natural seeing)	0.''5 at V, 0.''4 at K
θ_s (“core”)	$0.5 \times$ natural seeing, at V diffraction limit, near-IR
θ_s (“wings”)	$0.7 \times$ natural seeing
Strehl	0.05 in V, 0.7 in K
N_{pix}	Optimized ($n \times n \times n$)
N_{sky}	9

Table 14. Three-Mirror 20-Meter Telescope, F/11

Seeing (arcsec)	size (mm)	Resolution (12.5μ pixels)	Resolution \AA	Resolution R(6400 \AA)
1.000	0.156	12.48	8.52	751
0.500	0.078	6.24	4.26	1502
0.250	0.039	3.12	2.13	3004
0.125	0.020	1.56	1.06	6008

which is occulted out to a diameter of about 1.6 metres. For this case the central cell and the next two rings of cells in Fig. 16 are omitted. This leaves 36 cells arrayed in the next two rings. Two of the outermost spectrograph cells are shown in a Fig. 18. To produce a checkerboard arrangement so that a large contiguous area of sky can be observed one could use a 3-2-3 pattern in the four quadrants. Any other pattern or any number of cells could be chosen. A spectrograph cell for a two-mirror 30-metre telescope would be almost identical to the one designed here. In this case one would populate the central and innermost 3 rings in the hexagon pattern in Fig. 16. This would require 37 individual cells. With two exposures, offset by 0.5 cell diameters, no objects in the whole telescope field can be accessed.

9.4. Slitmasks

The size of the focal surface and its curvature and the large number of slitmasks required strongly suggest using a permanently mounted slitmask device in front of each cell. Just such a device, called MARS, has been designed by Roberts et al. (Proc. SPIE 4008, 968, 2000.) The device uses evenly spaced slits with a dead zone between each one. Each slit can be adjusted to a different width. Their test device used slits which were 4.5 mm long with a 1.0 mm dead zone between them. In our 20-metre design a 5 arcsec slit corresponds to 5.3 mm long while in the 30-metre case it is 10.9 mm long. Thus our requirements are quite close to their test device dimensions.

Such structures as shown in their paper would be mounted directly in front of each spectrograph cell. Since the slit setting devices can all run in parallel, they can all be set simultaneously. Since the telescope focal surfaces are curved, it will be necessary in the 30-metre telescope case to tilt the slit-mask to be tangent to the focal surface – the camera focal surface must also be tilted. The necessary tilt and focus adjustments can be made using piezoelectric actuators on the CCD mosaic mount. It will also be desirable to incorporate piezoelectric x-y translation on the CCD mosaic mount to correct for telescope tip-tilt changes.

One disadvantage of this system as compared with an off-telescope generated slit mask is the requirement that the slits be evenly spaced and all of the same length. This means that there is not necessarily an object on every slit, the situation depending on the density of candidate objects. Another disadvantage is that there is dead space between slits. For the test device above this amounts to 18 % and 8 % for the 20-metre and 30-metre designs, respectively.

9.5. Performance Expected

There are many glass-air surfaces in the optics of the spectrographs. With modern high-efficiency coatings these losses can be kept small. Vignetting by the optics only occurs for the light dispersed beyond the observed wavelength range and there will also be slight vignetting at the edge

of each cell field. With high efficiency coatings, our 20-metre spectrograph design has a throughput of about 42 % at 4000Å and more than 70 % above 6500Å. The other inefficiencies will come from the grating and the CCD quantum efficiency. The cells will have the same efficiency as current well designed low-resolution spectrographs.

Assuming we use a slit mask system and require 5 arcsec plus 1 arcsec dead space for each object to be observed, then each cell can have 49 and 29 slits for the 20-metre and 30-metre designs, respectively.

For the 20-metre design there are 36 cells and one can obtain up to 1764 spectra per exposure. For the 30-metre design we can implement 37 cells which then yields up to 1073 spectra per exposure. A single exposure can access half of the objects in the field. By shifting the telescope by about 0.5 cell diameters one can set on objects in the other half of the field. Two exposures can sample objects in the entire field of view of the 30-metre telescope. For the 20-metre case, the whole field is sampled except for a hole in the centre which occults 36 % of the total area.

9.6. Flexibility

During each exposure, about half the telescope focal surface is available for monitoring bright stars and making at least tip-tilt corrections. Since the seeing layer high in the atmosphere changes over the focal surface it is necessary to make tip-tilt corrections appropriate to each part of the field. There are plenty of stars from which to do this.

Cells need not all have the same configuration. For example, one could have a mixture of imaging and slitmask spectroscopy cells. In imaging cases there needs to be a way to change filters above the photometry cells where there is only limited space. With the very large focal surface considered, a mirror in front of the 30-metre Cassegrain focus could be used to intercept some part of the focal surface for some other another purpose such as integral-field spectroscopy or high resolution spectroscopy. In the case of the 20-metre 3-mirror design the light which would be lost behind the rear of the 45° flat could be diverted in another direction to provide an additional Cassegrain field with a 15 arcmin diameter.

9.7. Weight and Cost for the 20-Meter Telescope Spectrograph

One whole spectrograph cell is mounted in a standard 355.6 mm stainless steel tube 4.8 mm thick and 2.7 metres long. This tube weighs 113 kg and should be strong enough. For the design in Fig. 13 the weight of glass is 166 kg. The weight of the aluminum barrels which support the optics will be approximately 170 kg. Adding 10 kg for the Dewar for the CCDs, the total weight of a single spectrograph cell is about about 460 kg. Thirty six of these cells weigh 16,500 kg. To this must be added the weight of the structure which holds the 36 cells. This is likely to be an

additional 1000 kg.

The cost can be estimated because each spectrograph cell has 33% more optical components than the Gemini Multi-Object Spectrograph (GMOS) and the sizes are comparable. Scaling from GMOS, the glass will cost about \$250K. Allowing \$150K for figuring the glass, \$25K for a grism, and \$50K for fabricating the mountings, the cost per cell is about \$475K. For 36 cells the cost is \$17M. To this must be added the design costs, which are small compared with the total since only one cell is designed, and the cost of the slitmasks which are also small in comparison. No suitable ruling is available for the grism but since many are needed, the cost of a master would not be prohibitive. The cost of the 144 CCDs and 36 Dewars with piezoelectric actuators is likely to be at least \$1.0M. The total cost of the fully implemented spectrograph is likely to be at least US\$18M.

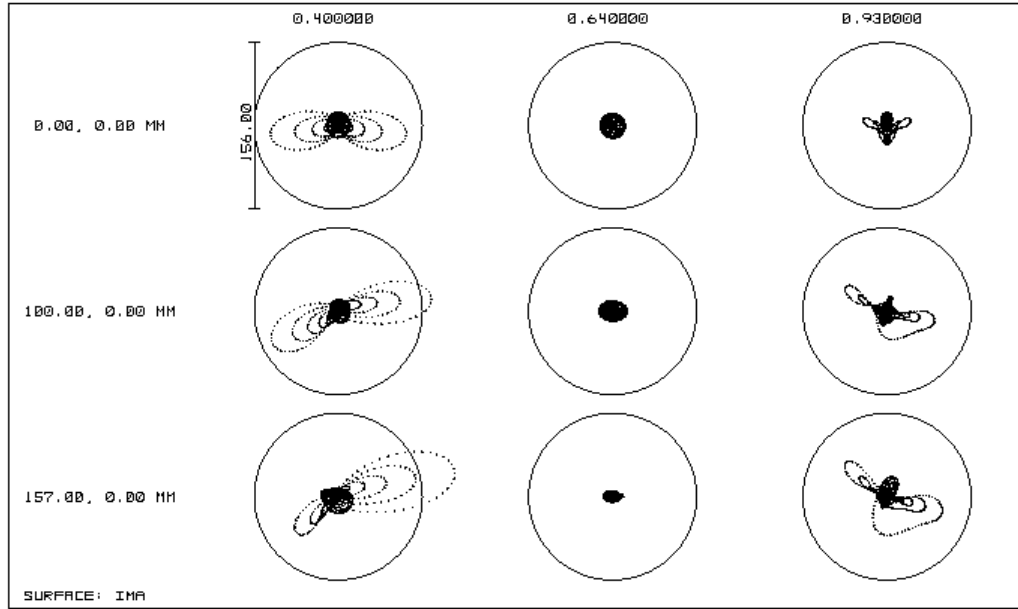


Fig. 14.— Spot diagrams in the camera focal plane at the centre, two thirds of the way out, and at the edge of the field. Spots are shown at 4000, 6400, and 9,300Å. The circle diameter is 1 arcsec or 156μ .

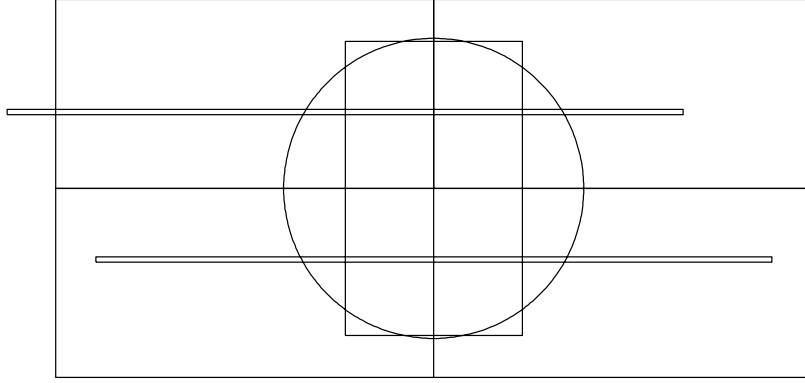


Fig. 15.— The layout in the camera surface. The circle is the clear unvignetted field. The 4 long rectangles are the four 2048x4096 pixel CCDs. The rectangle within the circle indicates where slits would be placed. The two long rectangles represent spectra which are 5000 Å long; one is centred, the other is at the extreme left edge of the slit field.

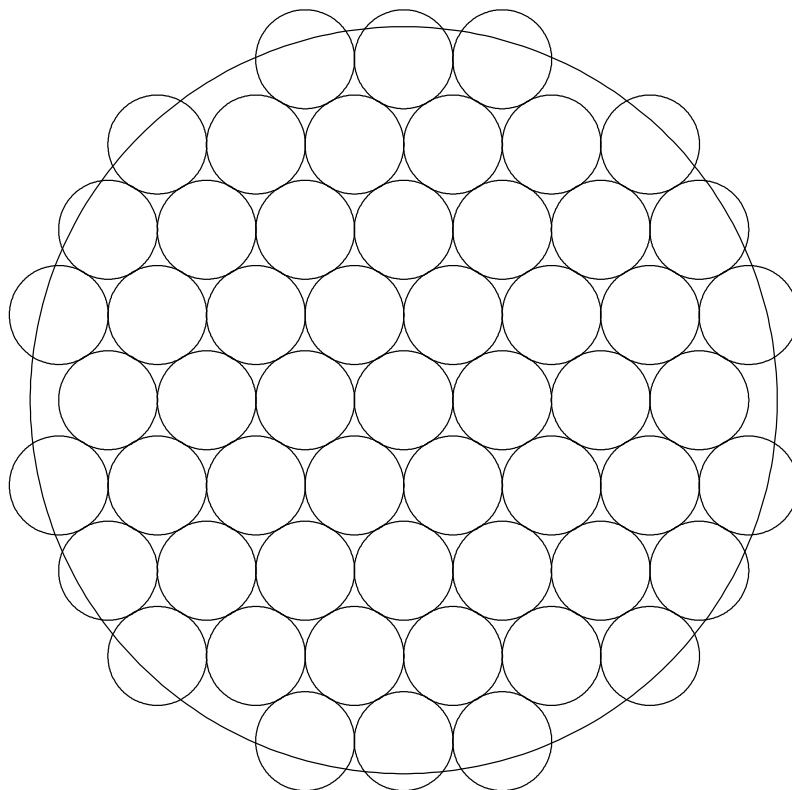


Fig. 16.— The layout of the 55 spectrograph cells in the telescope focal surface. In the 20-Meter 3-mirror telescope design the central and first two rings of cells are not used since the light has been occulted. The outside circle represents the 42 arcmin field.

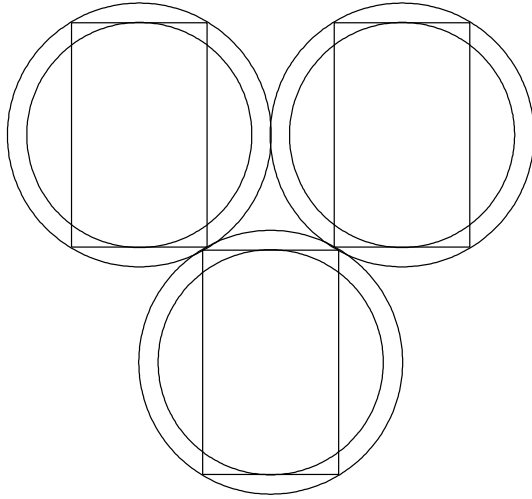


Fig. 17.— Three adjacent cells in the telescope focal surface. The outer circles are the mounting tube outside diameters, the inner circles the unvignetted fields. The rectangles are the areas where slits would be located. By offsetting the telescope one cell radius, objects in almost the entire field can be reached.

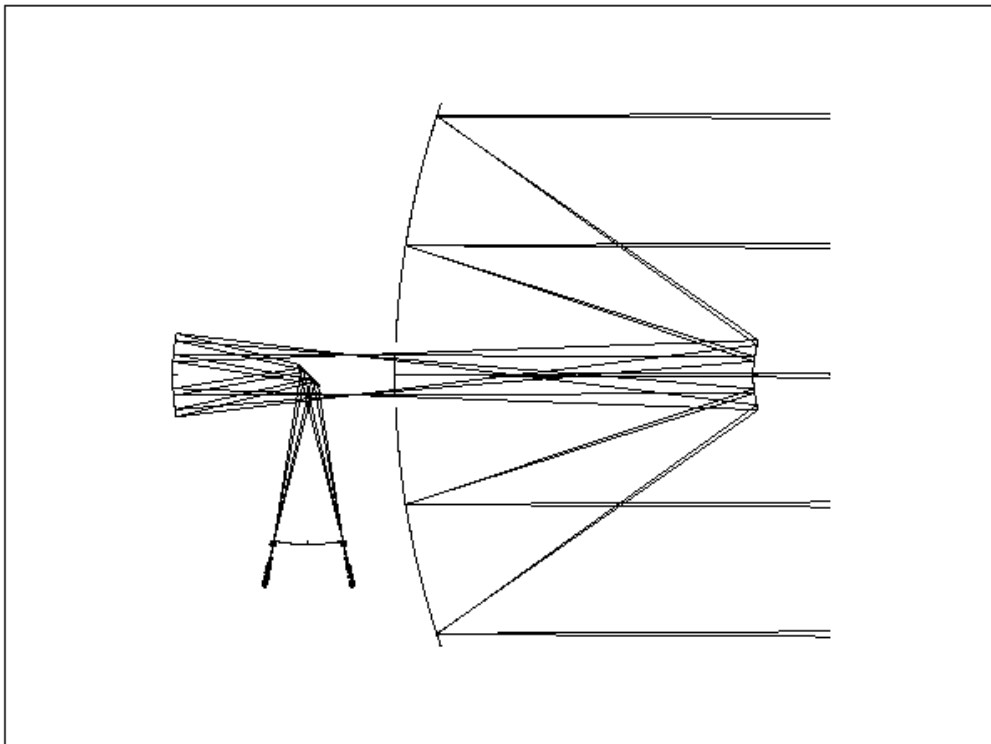


Fig. 18.— The layout of a Korsch 3-mirror 20-metre telescope design. The final focal plane is at the lower left. Two of the extreme spectrograph cells are shown to scale.